



### **Science Arts & Métiers (SAM)**

is an open access repository that collects the work of Arts et Métiers Institute of Technology researchers and makes it freely available over the web where possible.

This is an author-deposited version published in: <https://sam.ensam.eu>  
Handle ID: <http://hdl.handle.net/10985/12014>

#### **To cite this version :**

Antonin SANITAS, Marie BEDEL, Mohamed EL MANSORI, Nicolas CONIGLIO - Investigating surface roughness of ZE41 magnesium alloy cast by low-pressure sand casting process - International Journal of Advanced Manufacturing Technology - Vol. 92, n°5-8, p.1883-1891 - 2017

Any correspondence concerning this service should be sent to the repository

Administrator : [scienceouverte@ensam.eu](mailto:scienceouverte@ensam.eu)



# Investigating surface roughness of ZE41 magnesium alloy cast by low-pressure sand casting process

A. Sanitas<sup>1</sup> · N. Coniglio<sup>1</sup> · M. Bedel<sup>1</sup> · M. El Mansori<sup>1</sup>

Received: 6 January 2017 / Accepted: 10 March 2017  
© Springer-Verlag London 2017

**Abstract** The sand mold 3D printing technologies enable the manufacturing of molds with great dimensional accuracy. However, the roughness of as-cast components is higher when cast in a 3D printed mold rather than in a traditional sand mold. Coating the inner cavity is an efficient solution but can be costly and, in the narrowest cavities, not achievable. Finding a procedure to reduce the as-cast roughness without coating would ease the casting procedures. In the present work, surface analysis of ZE41 magnesium alloy is presented after being cast in 3D printed furan sand molds without coating using the low-pressure casting process. The molten metal temperature was measured during casting at different positions along the cast cavity. The as-cast surface roughness was correlated to the molten metal temperature and solid fraction at the time of contact against the sand mold surface.

**Keywords** Surface roughness · 3D printed mold · Low-pressure casting · Sand casting · Magnesium alloys

## 1 Introduction

The low-pressure sand casting (LPSC) process is suited for casting nonferrous alloys which are prone to oxidation (such as magnesium alloys). The filling velocity mastered during counter-gravity mold filling and the protective atmosphere

permanently present above the molten metal lower the amount of entrapped gas porosities and oxides in the cast components [1–3]. While the LPSC process has been widely studied for the aluminum casting industry, few investigations have been published about the LPSC of magnesium alloys [4–14].

The development in additive manufacturing, also referred to as 3D printing technology, widens the opportunities by improving dimensional accuracies for sand mold casting from functional prototypes to massive production [15, 16]. Nevertheless, casting a smooth as-cast surface using a 3D printed mold is challenging [17] but necessary to avoid expensive post-casting surface machining. While some studies measured the roughness of 3D printed mold castings cast by gravity process [17–22], no surface quality investigation has been found on 3D printed mold castings cast by the LPSC process. Moreover, the studies previously made on gravity castings investigated the effect of mold coating [17, 19], mold baking [19, 22], and alloy composition [20, 21] but were limited to aluminum alloys. Only one study has compared the roughness of a 3D printed mold with the induced as-cast surface roughness of Al-Si alloy [17]. Finally, no work has investigated the effect of molten metal temperature upon the surface roughness over the entire cast surface.

Coating the inner part of the mold cavity is commonly used to reduce efficiently the surface roughness of the as-cast components [17, 19], albeit the application of the coating is difficult, and even impossible, in the narrowest cavities that are obtainable today by 3D printing technologies. Enabling the as-cast roughness control without a coating application should therefore ease the foundry mold preparation.

The present work investigates the roughness transfer from mold to castings when poured into 3D printed furan sand molds without coating. Tests were carried out by casting Zr-refined ZE41 magnesium alloy in a cylinder-shaped cavity at different pressure ramps.

✉ N. Coniglio  
nicolas.coniglio@ensam.eu

<sup>1</sup> MSMP Laboratory, EA-7350, Arts et Metiers ParisTech, 2 cours des Arts et Metiers, 13617 Aix-en-Provence, France

## 2 Experimental setup

The proposed experimental approach is designed to investigate the transfer of the mold roughness signature to the as-cast surface when no coating is applied on the mold cavity. After the casting mold is printed, thermocouples are preplaced along the casting path to determine the molten metal temperature during casting. In addition, roughness measurements are performed upon the cast surfaces and mold specimens. The thermal and roughness data enable to correlate the as-cast surface roughness to the mold cavity roughness and the molten metal temperature.

### 2.1 Printing process

The sand molds used for the present study were printed by means of the ExOne S-Print Furan machine equipped with a  $800 \times 500 \times 400$ -mm job box. The printing process begins with the mixing of the sulfonic acid catalyst and inhibitor with 8 kg of sand particles and temporally stored in the mixing chamber. Sand layers of 280- $\mu$ m thickness are successively deposited in the *X-Y* plane with the addition of furfuryl alcohol binder spread by jet-printing nozzles. The process continues until the last slice of the mold is printed. The furan binder is cured at room temperature inside the job box for 1 h. The mold is then taken out of the job box and de-powdered. During the de-powdering, the sand particles not glued by the binder are removed with soft brushes and air-blown. No coating was spread in the inner part of the mold. The printing parameters, held constant throughout this study, are listed in Table 1. Printing was performed in a room maintained at a temperature of  $298 \pm 3$  K and relative humidity of  $40 \pm 10\%$ . The flexural strength and permeability of the printed sand molds are  $1.8 \pm 0.5$  MPa and  $75 \pm 7$  GP, respectively.

The mold design (Fig. 1) has been selected after preliminary tests. The mold cavity consists of 14-mm-diameter and 450-mm-long tubes along a direction orthogonal to the layer deposition direction. Bars are separated by 90 mm of furan sand mold to avoid thermal interactions. Each bar cavity was completely opened on the top side to avoid counter pressure ahead of the molten metal flow due to off-gassing of the binder.

### 2.2 Casting process

Bars were cast in the 3D printed molds using the Kurtz LPSC technology. Once wrought ingots of ZE41 were melted in the furnace, Zirmax<sup>®</sup> and rare earth hardener were added according to standard practice [23]. The cast alloy composition was measured prior to casting by ICP-OES spectroscopy using the Spectromaxx MX5M BT.

The sealed melt furnace was located below the mold support (vertical injection) with a steel rising tube of 70.9-mm

**Table 1** Printing parameters for S-Print furan process

Average sand grain size	140 $\mu$ m
AFS number	97
Activator content	0.18 wt%
Inhibitor content	0.4 wt%
Print head voltage	78 V
Layer thickness	280 $\mu$ m
Heating temperature	305 K
Furan drop spacing	140 $\mu$ m
Recoater speed	182 mm s <sup>-1</sup>

inside diameter. Superheat was set up at 115 K, which corresponds to a furnace temperature of 1033 K prior to casting. A dry Ar+2.0%SF<sub>6</sub> protective gas pressurized the furnace at a predefined pressure ramp above the molten metal, forcing the metal to rise through the rising tube in order to fill the mold

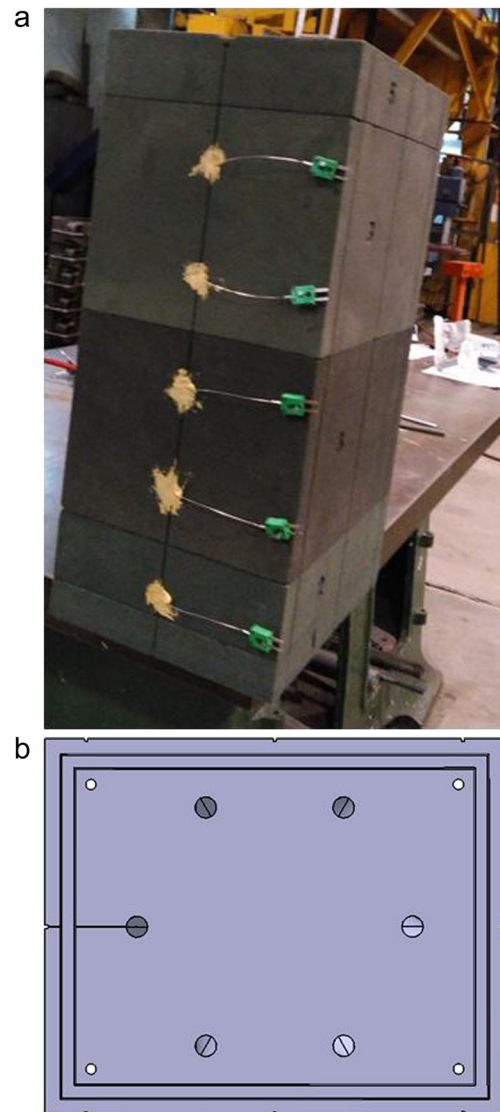


**Fig. 1** Furan sand mold. **a** Mold picture with embedded thermocouples and **b** top view of schematic design

cavity. The pressure ramp was maintained until the filling was blocked due to solidification. Three sets of experiments were performed at different casting pressure ramps: 3, 6, and  $15 \cdot 10^{-4} \text{ MPa s}^{-1}$ . Six bars were cast at each pressure ramp.

### 2.3 Metal characterization

A bar cast at  $15 \cdot 10^{-4} \text{ MPa s}^{-1}$  was instrumented by embedding thermocouples in the mold to measure the molten metal front temperature at various cavity positions. The ungrounded type-K thermocouples of 0.5-mm outer diameter (TCDirect) were placed at the centerline of the cylindrical cavity at respective distances of 0, 100, 200, and 300 mm from the start of the bar. Acquisition was performed with LabVIEW software at a 100-Hz frequency. Thermocouples response at 99%  $T_{\text{max}}$  was 1.2 s.

Following casting performance, two bar cross sections were cut for each casting pressure ramp condition. The resulting six cross sections were ground and mechanically polished to 1  $\mu\text{m}$  and then etched using a chemical solution (40 mL  $\text{HNO}_3$ , 30 mL  $\text{CH}_3\text{COOH}$ , 40 mL  $\text{H}_2\text{O}$ , and 120 mL ethanol). The microstructure was examined using optical metallography, and the grain size was measured using the line-intercept method of ASTM E112 [24], taking a mean value of six line-intercept measurements per cross section.

### 2.4 Roughness measurements

Profiles were measured along the mold and casting surfaces using the Morphoscan machine of Michalex with a 10- $\mu\text{m}$ -diameter diamond sphere applying a 0.4-mN load. Roughness parameters were calculated using a 50-mm sampling length, 1.6- $\mu\text{m}$  sampling rate, and high-pass filter with a cutoff value of 8 mm. These measuring conditions lead to  $R_a$  values between 10 and 80  $\mu\text{m}$ , validating the methodology according to NF EN ISO 4287 [25]. The calculated roughness parameters are the arithmetic average of absolute values ( $R_a$ ) and the maximal height of a profile ( $R_z$ ):

$$R_a = \frac{1}{N} \left( \sum_{i=1}^N |Y(x)| \right) \quad (1)$$

$$R_z = R_p - R_v \quad (2)$$

where  $Y(x)$  is the height at a position  $x$  along a surface of 8-mm length,  $R_v$  is the deepest valley, and  $R_p$  is the highest peak.

## 3 Results

### 3.1 Casting lengths

The lengths of the six cast bars were measured for the three studied filling pressure ramps. The bars were 89, 191, and

361-mm long when cast at 3, 6, and  $15 \cdot 10^{-4} \text{ MPa s}^{-1}$ , respectively. The scatter of bar lengths between the six bars cast at a same pressure ramp was within 3%. A linear relationship was observed between cast length ( $L$  in mm) and pressure ramp ( $\frac{dP}{dt}$  in  $\text{MPa s}^{-1}$ ) with a linear best-fitting curve given by the equation:

$$L = 2.524 \cdot 10^5 \frac{dP}{dt} (R^2 = 0.9508) \quad (4)$$

The increased pressure  $\frac{dP}{dt}$  applied on the melt surface by the dry Ar+2.0% $\text{SF}_6$  protective gas controls the height of the molten metal by the metalostatic pressure following the Pascal's pressure theory [26, 27]:

$$\frac{dP}{dt} = \rho \cdot g \cdot \frac{dh}{dt} = \rho \cdot g \cdot V_0 \quad (5)$$

where  $\rho$  is the molten ZE41 density ( $1570 \text{ kg m}^{-3}$ ) [28],  $g$  is the gravitational constant ( $9.8 \text{ m s}^{-2}$ ), and  $V_0$  is the metal front velocity (in  $\text{mm s}^{-1}$ ). Combining Eqs. 4 and 5 leads to Eq. 6:

$$L = 2.524 \cdot 10^5 \cdot \rho \cdot g \cdot V_0 \quad (6)$$

For sand casting conditions where the mold material controls the heat loss from the casting through both mold-metal interface and mold thermal diffusivity [29], the freezing time  $t_f$  is related to the cast length  $L$  and molten metal velocity  $V_0$  [30]:

$$L = t_f \cdot V_0 \quad (7)$$

Combining Eqs. 6 and 7 leads to the freezing time:

$$t_f = 2.524 \cdot 10^5 \cdot \rho \cdot g \quad (8)$$

Application of Eq. 8 to our data provides a freezing time of 3.9 s for Zr-refined ZE41 alloy in 3D printed furan sand molds. This freezing time depends upon the cast geometry that is for a 14-mm-diameter bar in this work.

### 3.2 Roughness measurements

The roughness profile of the sand mold was measured along the flowing direction of the molten metal flow (Fig. 2). The sand mold cavity prior to casting has a roughness of 32.9  $\mu\text{m}$  ( $R_a$ ) and 206.3  $\mu\text{m}$  ( $R_z$ ). The mold surface roughness is expected to influence the casting roughness by transferring partially its roughness signature to the casting surface.

The bars cast at  $3 \cdot 10^{-4} \text{ MPa s}^{-1}$  were too short for roughness measurements; subsequently, only the bars cast at 6 and  $15 \cdot 10^{-4} \text{ MPa s}^{-1}$  were used for roughness characterization.

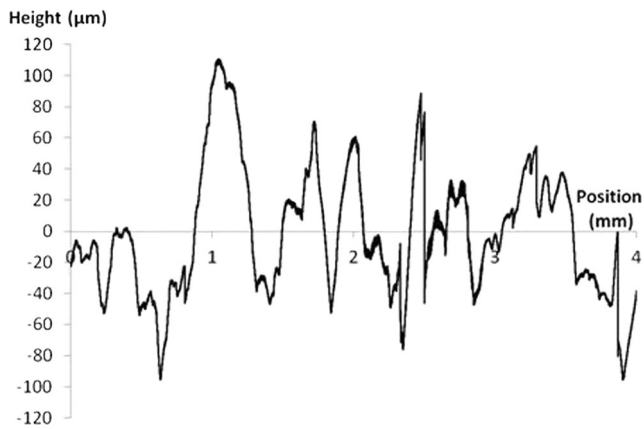


**Fig. 2** Roughness profile of sand mold surface prior to casting

The roughness profiles of the cast bars were measured from the bottom (Fig. 3a) to extremity (Fig. 3b), revealing a smoother surface near the bar extremity. Therefore, roughness parameters were calculated along the cast bar length for each individual 8-mm-long portion (Fig. 4). Both  $R_a$  and  $R_z$  roughness values are smaller near the end than the start of the cast bars, meaning that the later the molten metal spreads on the mold surface, the smaller the surface roughness value is.

### 3.3 Microstructure characterization

The cast alloy composition measured by ICP-OES spectroscopy revealed that the main alloying elements are 3.7 wt% Zn, 0.7 wt% Zr, and 1.3 wt% RE. Thermocouples embedded into the mold cavity indicated a cooling rate of approximately 4 °C/s during the solidification. Cross sections observed by

optical microscopy did not evidence an effect of casting pressure ramp upon the grain size, which was expected as cooling rate and composition remain constant. The line-intercept method on optical metallographic images provides an average grain size of 37.6 μm with a standard deviation of 4.0 μm.

The cast metal microstructure (Fig. 5) was similar for the three pressure ramp conditions. The cast microstructure shows α-Mg solid solution outlined by the T-phase ( $Mg_7Zn_3RE$ ). These phases have been labeled based upon description available in the literature [31–33] and upon Thermo-Calc thermal analysis performed in this study.

### 3.4 Thermal analysis

The partial transfer of mold roughness to casting surfaces was afterwards investigated in regards to the molten metal thermal history. The solidification path of the Zr-refined ZE41 alloy was calculated using Thermo-Calc software under equilibrium conditions (Lever rule), using the solute composition measured by ICP-OES spectroscopy. The solidification path is plotted in Fig. 6. According to the simulation, solidification of the Zr-refined ZE41 starts at 950 K, well above the liquidus of Zr-free ZE41 (918 K). This agrees with other works that observed Zr-rich intermetallic particles present as a nucleus at the α-Mg grain center [31]. The solid fraction of the Zr-refined ZE41 is only 0.01 at 918 K and the solidus temperature is 824 K.

One bar cast at  $15 \cdot 10^{-4} \text{ MPa s}^{-1}$  was instrumented by embedding thermocouples in the mold to measure the molten metal front temperature at various cavity positions. From the

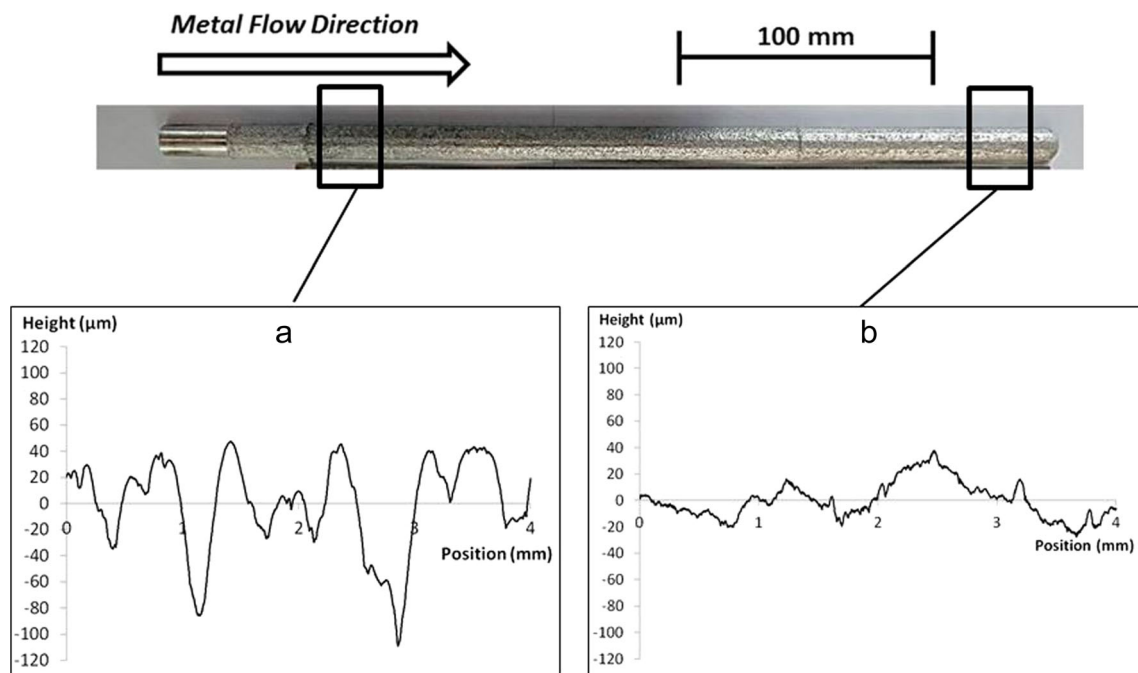


**Fig. 3** Overview of ZE41 cast bar at  $15 \cdot 10^{-4} \text{ MPa s}^{-1}$  ramp with superposed roughness profiles at **a** 80 and **b** 350 mm from bar bottom



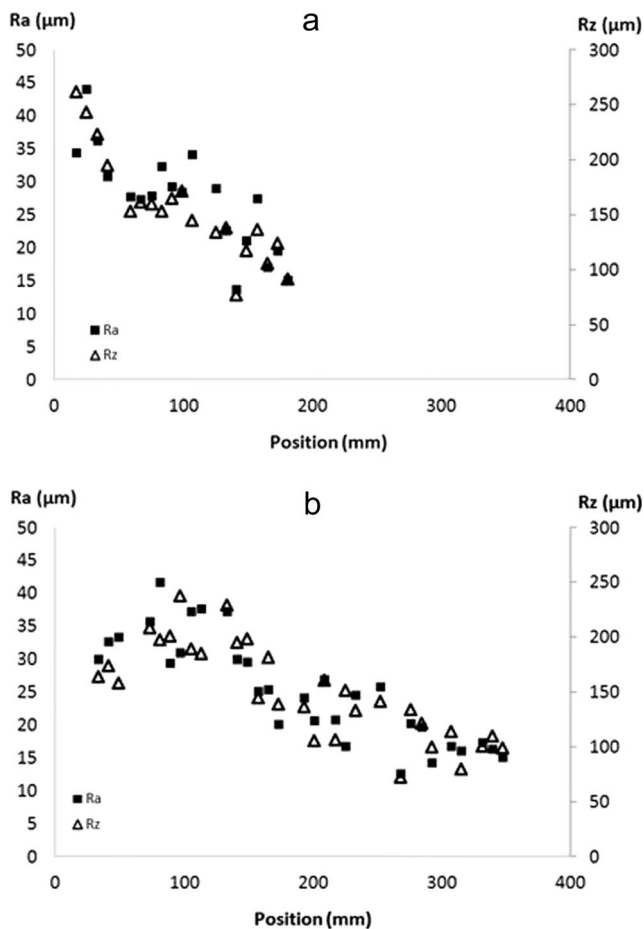


**Fig. 4** Roughness profiles of ZE41 cast bar at **a**  $6 \cdot 10^{-4}$  MPa s $^{-1}$  and **b**  $15 \cdot 10^{-4}$  MPa s $^{-1}$  along cast bar length

four measured temperature evolutions, the melt front temperature could be extrapolated along the bar length. This

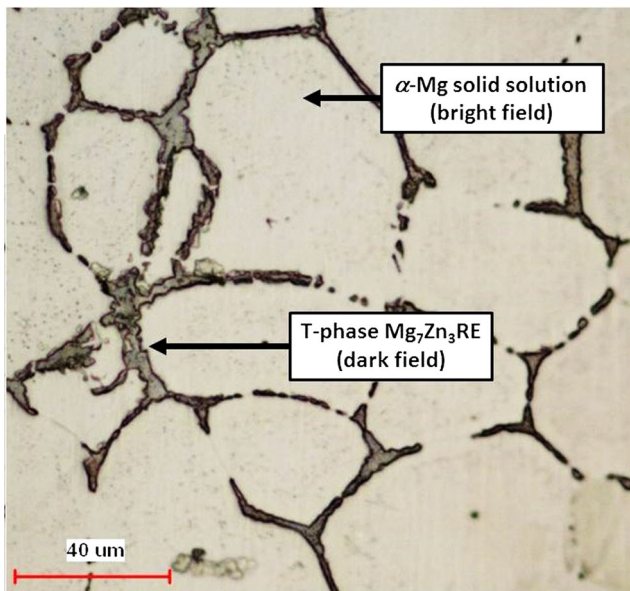


**Fig. 5** Alloy ZE41 solidification microstructure cast at  $15 \cdot 10^{-4}$  MPa s $^{-1}$  highlighting the different phases

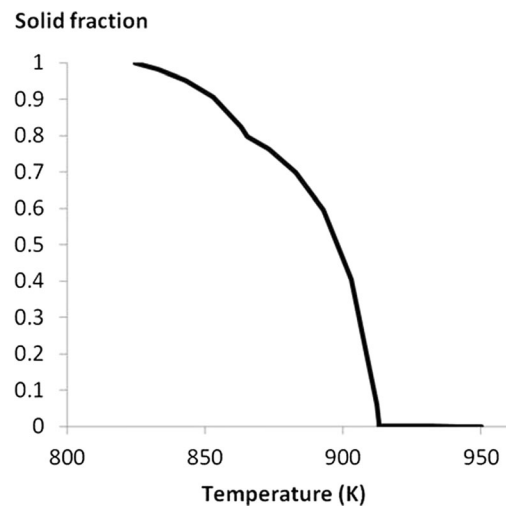


**Fig. 6** Solid fraction versus temperature curve for Zr-refined ZE41 alloy

extrapolated measured temperature profile was combined with the calculated solidification path in order to extract the solid fraction of the melt front until filling blocking (Fig. 7). The metal, fully liquid at 956 K when entering the tube cavity, cools and solidifies during filling until it reaches 903 K and 0.41 of solid fraction at the instant filling blocks.

The positions along the cast bars were converted into temperature values of the molten metal front (Fig. 8). Roughness values for  $6$  and  $15 \cdot 10^{-4}$  MPa s $^{-1}$  cast bars show similar trends and values when plotting these roughness parameters as a function of temperature (Fig. 8a, b) and solid fraction (Fig. 8c, d) variations at the melt front. Table 2 details the roughness parameter variations along the dashed trend lines superimposed to the measured data in Fig. 8.

Above 908 K and below 0.22 solid fraction, the roughness parameters maintain constant values, albeit the data scatter is large. The large scatter of the roughness values arises from cavity surface variations originally caused by the size distribution rather a single size of the sand grains used for mold manufacturing and the brush and air-blown cleaning processes

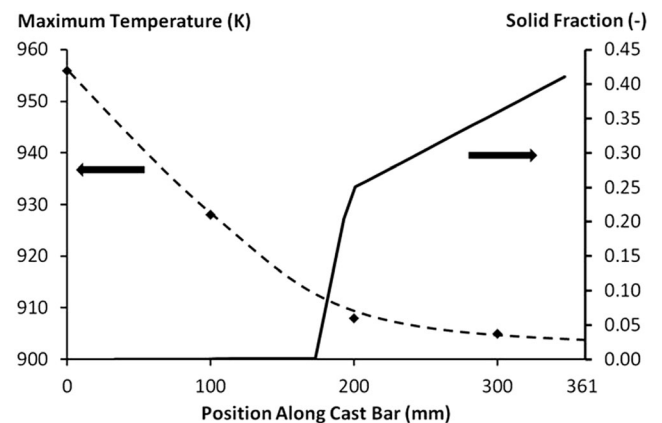


**Fig. 7** Melt front temperature (*dashed line*) and corresponding solid fraction (*solid line*) from bottom (0 mm) to extremity (361 mm) of bar cast at  $15 \cdot 10^{-4}$  MPa s $^{-1}$

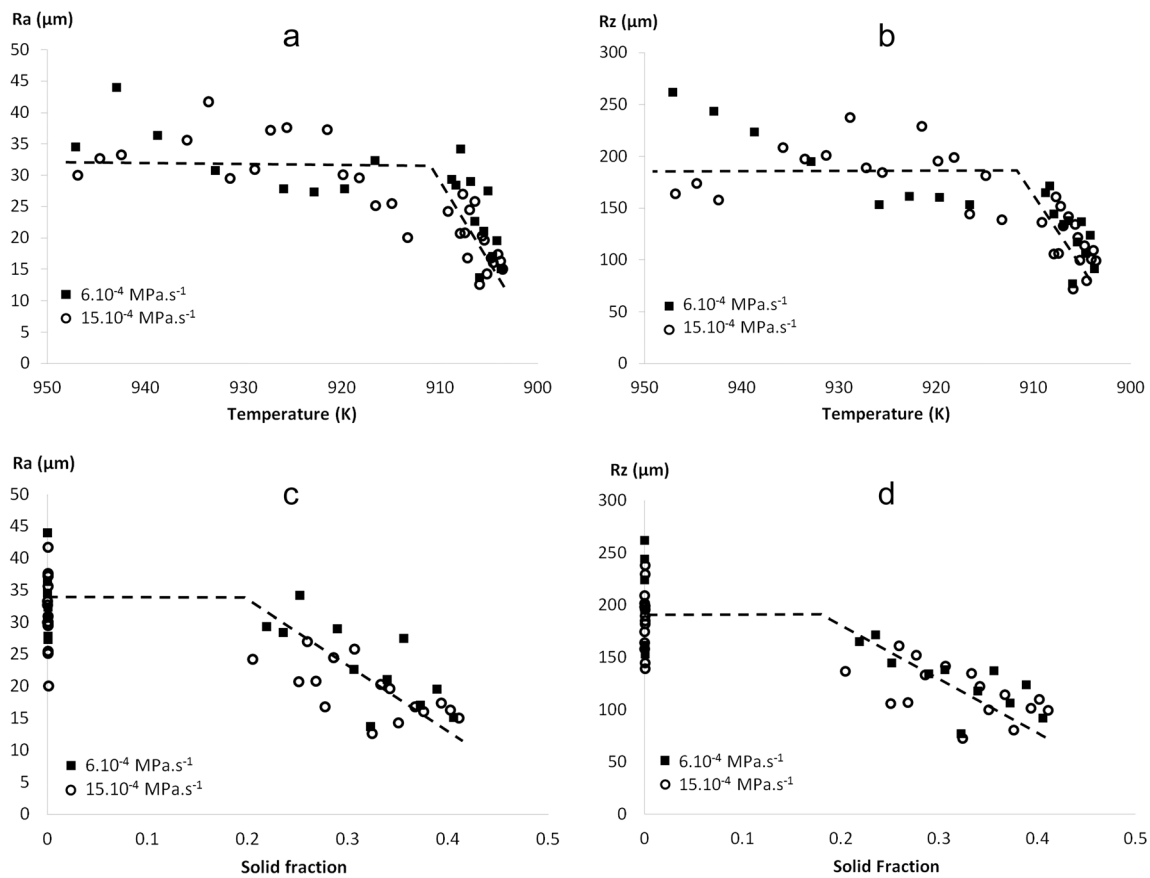


**Fig. 8** Relationship between roughness (a, c)  $R_a$  and (b, d)  $R_z$  profiles of ZE41 cast bars and molten front (a, b) temperature and (c, d) solid fraction

that leave an additional surface signature upon the mold cavity.

Taking the 30 measurements performed above 908 K, the roughness has average values of  $31.4 \mu\text{m}$  ( $R_a$ ) and  $183.6 \mu\text{m}$  ( $R_z$ ) with an interval of 95% confidence of 1.7 and  $10.9 \mu\text{m}$ , respectively, according to the Student  $t$  distribution law. Therefore, above 908 K, the casting surface roughness roughly matches the mold surface roughness. However, further cooling of the molten front induces a progressive drop in the as-cast roughness values that finally attain near the bar extremity values of  $16.8 \pm 1.7 \mu\text{m}$  ( $R_a$ ) and  $105.2 \pm 11.0 \mu\text{m}$  ( $R_z$ ).

#### 4 Discussion

The present work reveals that the cast surface roughness roughly matches the mold surface roughness, in agreement

with other works from literature [17, 34]. While only the present work has performed low-pressure sand casting, the as-cast  $R_a$  roughness values in this work (between 16.8 and  $44.0 \mu\text{m}$ ) are in the same order of magnitude than the one obtained by gravity casting processes in 3D printed sand molds (between 4.6 and  $47.1 \mu\text{m}$ ) [17–22, 35]. These previous works proved that the casting roughness depends upon the cast metal [20, 21], the mold surface preparation [17, 19], and mold baking conditions [19], but none has investigated the metal temperature effect.

The present work brings a novel viewpoint by evidencing a strong effect of metal temperature during filling on the as-cast roughness. Casting at low temperatures reduces the roughness of the as-cast components, which adds to the advantageous greater mechanical properties observed by Fu et al. [4]. However, the roughness dependency upon the molten metal temperature induces a roughness variation over the entire cast

**Table 2** Relationship between roughness parameters ( $R_a$ ,  $R_z$ ) and molten metal conditions (solid fraction  $f_S$  and temperature  $T$ )

$R_a$ ( $\mu\text{m}$ )	$R_z$ ( $\mu\text{m}$ )	Range of validity
31.4	183.6	$T < 908 \text{ K}$
$2.75 \cdot T - 2470.8$ ( $R^2 = 0.65$ )	$10.68 \cdot T - 9555$ ( $R^2 = 0.46$ )	$903 \text{ K} < T < 908 \text{ K}$
31.4	183.6	$0.22 < f_S$
$-74.45 \cdot f_S + 45.4$ ( $R^2 = 0.65$ )	$-288.67 \cdot f_S + 214.6$ ( $R^2 = 0.46$ )	$0.22 < f_S < 0.41$

surface. The threshold 908 K temperature, below which roughness drops, is reached at the molten metal front after 1.8 s of filling among the total filling duration of 3.9 s. Therefore, the present work suggests some rules for the conception of LPSC molds. If some casting parts require very low roughness values, these parts should be located in mold cavities being filled last, usually located at the top of the mold for LPSC conditions. However, if the roughness homogeneity over the entire casting surface is the most important quality factor, the filling of a 14-mm-diameter mold cavity must be completed within 1.8 s after the filling begins. Similar works will be conducted on other geometries to investigate the filling time dependency of Zr-refined ZE41 alloy on the mold cavity geometry.

The surface roughness has been evaluated in the vertical upwards casting conditions. While the roughness continuously decreases in the  $6 \cdot 10^{-4}$ -MPa  $s^{-1}$  casting conditions, it is initially constant for the  $15 \cdot 10^{-4}$ -MPa  $s^{-1}$  casting ramp. This suggests that the hydrostatic pressure for the LPSC process with magnesium alloys, which varies up to  $6 \cdot 10^{-3}$  MPa for the 360-mm-long bars cast at  $15 \cdot 10^{-4}$  MPa  $s^{-1}$ , has little effect on the cast roughness in regards to the scatter of the data. Therefore, the measurements should not be significantly affected if casting is performed in the inclined or horizontal directions. This is in agreement with the present work hypothesis that the as-cast roughness depends mainly on the molten metal temperature at the time of contact with the mold and little on the molten metal hydrostatic pressure.

The analysis of the transition in as-cast roughness from constant high values to continuously reducing values needs further work. A smaller as-cast roughness suggests a lower penetration of the molten metal into the mold asperities that is associated to a smaller wettability. The wetting by a liquid of a rough solid surface, such as the mold cavity, depends, among other factors, upon the liquid–gas surface tension and the contact angle of the liquid over a flat surface of the same solid substrate [36]. The smaller wettability of colder molten metal may possibly arise from an increase in wetting angle, leading to a change from the Cassie to Wenzel wetting mechanism [37, 38]. According to the Thomas Young wetting model, a larger liquid–solid contact angle can be due to an increase in liquid–gas surface tension  $\gamma_{LG}$  from its value at the liquid state (552–572 mN  $m^{-1}$  for molten magnesium [39]. However, this hypothesis may possibly not be applicable in this work because the considered molten metal is in reality a semisolid metal with increasing solid fraction as it cools down.

The phenomenon of wetting for liquids becomes more complex when solidification takes place simultaneously. The solidifying metal progressively changes from a liquid to a solid behavior for solid fractions from 0 to 1. The semisolid metal behaves like a liquid below a threshold solid fraction (coherency point) above which the semisolid metal exhibits

shear strength due to the entanglement of the solid particles. Later, the semisolid metal acquires some tensile strength by intergrain solid bridging (coalescence point). In the present castings, the threshold solid fraction from which roughness drops is believed to represent the initial shear resistance of the semisolid metal that hinders the liquid penetration into the asperities. It is followed at the end of the cast bars by a blockage of the liquid front when the grain coalescence is sufficient [30]. In the present case, according to the performed castings, the coherency and coalescence points for the ZE41 magnesium alloy are determined at solid fractions of 0.22 and 0.41, respectively.

Determining the coherency and coalescence points of an alloy is of great importance for characterizing the semisolid rheological properties with applications in several solidification-related domains such as solidification cracking modeling [40–45] and stir casting process understanding [46–48]. Experimental measurement of these two points could be implemented in the corresponding models when used in combination with casting simulations. Nevertheless, these two points are usually determined by simulation as experimental measurements are difficult to perform.

The experimental attempts for the determination of coherency and coalescence points have been performed through complex tensile and shear tests. Tensile tests [49–52] determine the tensile strength to failure in the semisolid state, and thus the coalescence point, but are difficult to carry out because of the small stresses and large deformations involved. On the other hand, the shear tests [53, 54] measure the shear resistance of the semisolid metal by sliding one part of the mold relatively to another [53] or by rotating a four-blade vane into a solidifying metal [54]. When undergoing solidification, the coherency temperature is evidenced in those shear tests by a sharp deviation of the strength–temperature curve. All these tests are however difficult to perform and may possibly be not representative of the alloy semisolid behavior when cast in 3D printed furan sand molds. The present work proposes a simple methodology to identify the solid fraction at the coherency and coalescence points for the solidification conditions in the furan sand molds, corresponding to a drop in roughness and filling blockage, respectively. Nevertheless, it requires the post-casting measurement of the roughness of the as-cast surface and an in situ thermal analysis.

## 5 Conclusion

The present work focused on the correlation between molten metal temperature and final casting roughness values for Zr-refined ZE41 magnesium alloy cast in 3D printed furan sand molds using the low-pressure casting process. The casting roughness is shown to be dependent upon the molten metal temperature and solid fraction at the instant of contact.



Roughness values drop when molten metal temperature is below a temperature of 908 K corresponding to a solid fraction of 0.22. Therefore, the mold cavity elements filled at last would possess the lowest roughness values. The ability to measure a solid fraction for the wetting behavior transition has led to the proposal of using the casting procedure of the present work as an experimental setup for coherency point measurement. Future work will aim at investigating the study of the solidification and crystallization of Zr-refined ZE41 alloys with the DSC method in order to provide experimental solid fraction–temperature curves and investigate the liquid and semisolid behavior of other magnesium alloys.

**Acknowledgements** The authors acknowledge the contribution of colleagues. Thanks are due to J. Bourgeois and J. Nègre of the Arts et Métiers ParisTech for their technical support and T. Boden and R. Baird of Magnesium Elektron for their advices. The authors are also gratefully acknowledged to INOVSYs platform for providing the equipment used for this work.

## References

- Duan J, Majjer D, Cockcroft S, Reilly C (2013) Development of a 3D filling model of low-pressure die-cast aluminum alloy wheels. *Metall Mater Trans A* 44:5304–5315. doi:10.1007/s11661-013-1654-6
- Bonollo F, Urban J, Bonatto B, Botter M (2005) Gravity and low pressure die casting of aluminium alloys: a technical and economical benchmark. *La Metall Ital* 23–32.
- Bichler L, Ravindran C (2010) Characterization of fold defects in AZ91D and AE42 magnesium alloy permanent mold castings. *Mater Charact* 61:296–304. doi:10.1016/j.matchar.2009.12.011
- Fu P, Luo A, Jiang H et al (2008) Low-pressure die casting of magnesium alloy AM50: response to process parameters. *J Mater Process Technol* 205:224–234. doi:10.1016/j.jmatprotec.2007.11.111
- Luo A (2013) Magnesium casting technology for structural applications. *J Magnes Alloy* 1:2–22. doi:10.1016/j.jma.2013.02.002
- Gertsman VY, Li J, Xu S et al (2005) Microstructure and second-phase particles in low- and high-pressure die-cast magnesium alloy AM50. *Metall Mater Trans A* 36:1989–1997. doi:10.1007/s11661-005-0319-5
- Chiesa F, Morin G, Duchesne B, Baril J (2011) Comparing low pressure and gravity permanent mold casting of magnesium AZ91E and aluminium A356. *Trans Am Foundry Soc* 119:441–452
- Thomson JP, Xu S, Sadayappan M et al (2004) Low pressure casting of magnesium alloys AZ91 and AM50. 985–994
- Sadayappan M, Thomson JP, Sahoo M (2006) Casting fluidity of magnesium alloy AZ91 in gravity and low pressure casting. *AFS Trans*:747–754
- Edler FJ, Lagrené G, Siepe R (2006) Thin-walled Mg structural parts by a low-pressure sand casting process. In: *Magnes. Alloy. Their Appl.* Wiley-VCH Verlag GmbH & Co. KGaA, Weinheim, pp 553–557
- Li Z, Fu P, Peng L et al (2013) Influence of solution temperature on fatigue behavior of AM-SC1 cast magnesium alloy. *Mater Sci Eng A* 565:250–257. doi:10.1016/j.msea.2012.12.035
- Li Y, Wu G, Chen A et al (2015) Effects of Gd and Zr additions on the microstructures and high-temperature mechanical behavior of Mg–Gd–Y–Zr magnesium alloys in the product form of a large structural casting. *J Mater Res* 30:3461–3473. doi:10.1557/jmr.2015.306
- Wang Y, Li D, Peng Y, Zeng X (2007) Numerical simulation of low pressure die casting of magnesium wheel. *Int J Adv Manuf Technol* 32:257–264. doi:10.1007/s00170-005-0325-1
- Peng Y, Wang Y, Li D, Zeng X (2004) The simulation of magnesium wheel low pressure die casting based on PAM-CAST TM. *Proceedings of AIP conference* 712 1248:1248–1252. doi: 10.1063/1.1766700
- Almaghariz ES, Conner BP, Lenner L et al (2016) Quantifying the role of part design complexity in using 3D sand printing for molds and cores. *Int J Met* 10:240–252. doi:10.1007/s40962-016-0027-5
- Singh R (2011) Process capability study of rapid casting solution for aluminium alloys using three-dimensional printing. *Int J Automot Mech Eng* 4:398–405
- Nyembwe K, de Beer DJ, van der Walt JG, Bhero S (2012) Assessment of surface finish and dimensional accuracy of tools. *South African J Ind Eng* 23:130–143
- Bassoli E, Gatto A, Iuliano L, Violante MG (2007) 3D printing technique applied to rapid casting. *Rapid Prototyp J* 13:148–155. doi:10.1108/13552540710750898
- Bobby SS (2014) A preliminary investigation of gypsum bonded moulds by three dimensional printing. *IJRET Int J Res Eng Technol* 3:501–507
- Gill SS, Kaplas M (2011) Efficacy of powder-based three-dimensional printing (3DP) technologies for rapid casting of light alloys. *Int J Adv Manuf Technol* 52:53–64. doi:10.1007/s00170-010-2716-1
- Hościlo B, Kaczyński R, Skorulski G (2014) Rapid prototyping technology using for casting process of mini turbine runner. *Arch Foundry Eng* 14:83–86
- Snelling D, Blount H, Forman C, et al (2013) The effects of 3D printed molds on metal castings. *Solid Free Fabr Symp* 827–845
- Friedrich HE, Mordike BL (2006a) *Magnesium technology: metallurgy, design data, applications*. Springer, Berlin
- ASTM (2004) ASTM E 112-96(2004) standard test methods for determining average grain size
- AFNOR (1998) NF EN ISO 4287/A1
- Hogg JC, Westengen H, Albright DL (1991) Low pressure sand casting of magnesium alloys. *Proc. Int. Symp. Extr. Refin. Fabr. Light Met.* Ottawa, Ontario
- Liu S-G, Cao F-Y, Zhao X-Y et al (2015) Characteristics of mold filling and entrainment of oxide film in low pressure casting of A356 alloy. *Mater Sci Eng A* 626:159–164. doi:10.1016/j.msea.2014.12.058
- Lide DR (2000) *Handbook of chemistry and physics: a ready-reference book chemical and physical data*, 81st ed. CRC-Press
- Campbell J (2003) *CASTINGS*. doi: 10.1007/s13398014017372
- Flemings MC (1964) Fluidity of metals—techniques for producing ultra-thin section castings. *Br Foundrym*:312–325
- Neil WC, Forsyth M, Howlett PC et al (2009) Corrosion of magnesium alloy ZE41—the role of microstructural features. *Corros Sci* 51:387–394. doi:10.1016/j.corsci.2008.11.005
- Wang Y, Wu G, Liu W et al (2014) Effects of chemical composition on the microstructure and mechanical properties of gravity cast Mg–x Zn–y RE–Zr alloy. *Mater Sci Eng A* 594:52–61. doi:10.1016/j.msea.2013.11.040
- Friedrich H, Mordike B (2006b) *Magnesium technology: metallurgy, design data, applications*
- Lannutti JJ, Mobley CE (2003) *Improvements in Sand Mold/Core Technology: Effects on Casting Finish*. Columbus, OH 43210
- Chhabra M (2011) Experimental investigation of pattern-less casting solution using additive manufacturing technique. 1:17–25
- de Gennes P-G, Brochard-Wyart F, Quéré D (2004) *Capillarity and wetting phenomena*. doi: 10.1007/978-0-387-21656-0

37. Bico J, Tordeux C, Quéré D (2001) Rough wetting. *EPL (Europhysics Lett)* 55:214
38. Carbone G, Mangialardi L (2005) Hydrophobic properties of a wavy rough substrate. *Eur Phys J E* 16:67–76. doi:[10.1140/epje/e2005-00008-y](https://doi.org/10.1140/epje/e2005-00008-y)
39. Flint O (1965) Surface tension of liquid metals. *J Nucl Mater* 16: 233–248. doi:[10.1016/0022-3115\(65\)90113-3](https://doi.org/10.1016/0022-3115(65)90113-3)
40. Coniglio N, Cross CE (2013) Initiation and growth mechanisms for weld solidification cracking. *Int Mater Rev* 58:375–397. doi:[10.1179/1743280413Y.0000000020](https://doi.org/10.1179/1743280413Y.0000000020)
41. Eskin DG, Suyitno, Katgerman L (2004) Mechanical properties in the semi-solid state and hot tearing of aluminium alloys. *Prog Mater Sci* 49:629–711. doi:[10.1016/S0079-6425\(03\)00037-9](https://doi.org/10.1016/S0079-6425(03)00037-9)
42. Eskin DG, Katgerman L (2007) A quest for a new hot tearing criterion. *Metall Mater Trans A* 38:1511–1519. doi:[10.1007/s11661-007-9169-7](https://doi.org/10.1007/s11661-007-9169-7)
43. Suyitno KWH, Katgerman L (2005) Hot tearing criteria evaluation for direct-chill casting of an Al-4.5 pct Cu alloy. *Metall Mater Trans A* 36:1537–1546. doi:[10.1007/s11661-005-0245-6](https://doi.org/10.1007/s11661-005-0245-6)
44. Cross CE (2005) On the origin of weld solidification cracking. In: *Hot cracking phenomena in welds*. Springer-Verlag, Berlin, pp 3–18
45. Cross CE, Coniglio N (2008) Weld solidification cracking: critical conditions for Crack initiation and growth. In: *Hot cracking phenomena in welds II*. Springer, Berlin, pp 47–66
46. Brabazon D, Browne D, Carr A (2002) Mechanical stir casting of aluminium alloys from the mushy state: process, microstructure and mechanical properties. *Mater Sci Eng A* 326:370–381. doi:[10.1016/S0921-5093\(01\)01832-9](https://doi.org/10.1016/S0921-5093(01)01832-9)
47. Dwivedi SP, Gupta B, Chaudhary D (2014) The effect of process parameters on mechanical stir casting process. *NIET J Eng Technol* 1
48. Koli DK, Agnihotri G, Purohit R (2015) Influence of ultrasonic assisted stir casting on mechanical properties of Al6061-nano Al<sub>2</sub>O<sub>3</sub> composites. *Mater Today Proc* 2:3017–3026. doi:[10.1016/j.matpr.2015.07.286](https://doi.org/10.1016/j.matpr.2015.07.286)
49. Dickhaus CH, Ohm L, Engler S (1994) Mechanical properties of solidifying shells of aluminium alloys. *AFS Trans* 101:677–684
50. Pumphrey WI, Moore DC (1948) A consideration of the nature of brittleness at temperatures below the solidus in castings and welds in aluminium alloys. *J Inst Met* 75:257–267
51. Singer ARE, Cottrell SC (1946) Properties of the aluminium-silicon alloys at temperatures in the region of the solidus. *J Inst Met* 73:33–54
52. Lu Z-J, Evans WJ, Parker JD, Birley S (1996) Simulation of microstructure and liquation cracking in 7017 aluminium alloy. *Mater Sci Eng A* 220:1–7. doi:[10.1016/S0921-5093\(96\)10458-5](https://doi.org/10.1016/S0921-5093(96)10458-5)
53. Metz SA, Flemings MC (1970) A fundamental study of hot tearing. Des Plaines, Illinois
54. Dahle AK, Arnberg L (1997) Development of strength in solidifying aluminium alloys. *Acta Mater* 45:547–559. doi:[10.1016/S1359-6454\(96\)00203-0](https://doi.org/10.1016/S1359-6454(96)00203-0)